

# Rock Mass Stability Investigation Around Tunnels in an Underground Mine in USA

Yan Xing · P. H. S. W. Kulatilake · L. A. Sandbak

Received: 2 March 2016 / Accepted: 27 August 2016 / Published online: 3 September 2016  
© Springer International Publishing Switzerland 2016

**Abstract** Stability and deformation of rock masses around tunnels in underground mines play significant roles on the safety and efficient exploitation of the ore body. Therefore, understanding of geomechanical behavior around underground excavations is important and necessary. In this study, a three-dimensional numerical model was built and stress analyses were performed by using 3DEC software for an underground mine in USA using the available information on stratigraphy, geological structures and mechanical properties of rock masses and discontinuities. Investigations were conducted to study the effect of the lateral stress ratio ( $K_0$ ), material constitutive models, boundary conditions and rock support system on the stability of rock masses around the tunnels. Results of the stress,

displacement, failure zone, accumulated plastic shear strain and post-failure cohesion distributions were obtained for these cases. Finally, comparisons of the deformation were made between the field deformation measurements and numerical simulations.

**Keywords** Underground mine · Rock mass stability · 3DEC · Strain-softening · Support system

## 1 Introduction

Stability of underground excavations, such as tunnels and caverns, play important roles in ensuring the overall stability of mine structures, as well as providing safety working places for ore production. Instability of underground excavations can arise due to a number of factors. As one of the major factors, discontinuities including faults, joints, bedding planes, shear zones and dykes could significantly weaken the strength of rock masses (Aydan et al. 1997; Wu and Kulatilake 2012a, b). As excavation goes down deeper, the problem of high in situ stress is encountered, and the most unfavorable situation for tunnels is excavating in the direction perpendicular to the maximum horizontal principal stress direction (Wang et al. 2012; Kulatilake et al. 2013). In addition, hydrological conditions, excavation geometries, soft rock strata, and other factors, are likely to make the problem more complicated and challenging (Chen et al. 1997; Liu et al. 2012; Kulatilake et al. 2013).

---

Y. Xing  
Department of Mining and Geological Engineering,  
University of Arizona, Tucson, AZ 85721, USA  
e-mail: yxing@email.arizona.edu

Y. Xing  
State Key Laboratory for Geomechanics and Deep  
Underground Engineering, China University of Mining  
and Technology, Xuzhou 221116, China

P. H. S. W. Kulatilake (✉)  
Rock Mass Modeling and Computational Rock Mechanics  
Laboratories, University of Arizona, Tucson, AZ 85721,  
USA  
e-mail: kulatila@u.arizona.edu

L. A. Sandbak  
Barrick Gold Inc., Golconda, NV 89414, USA

Therefore, it is necessary to understand the rock mass behavior around underground excavations and to come up with design procedures which could eliminate or minimize possible problems. Support systems have been used to improve these unsatisfactory situations for many years (Hoek et al. 1995; Barton et al. 1974; Nickson 1992). A summary of different support systems such as shotcrete linings, steel arches, mechanically anchored rock bolts, cable bolts and grouted rock bolts, as well as their applicability in underground excavations are discussed by Hoek et al. (1995).

In this paper, stability of an underground mine in USA is investigated. The ore body in this mine is dipping approximately  $25^{\circ}$ – $45^{\circ}$  with a relatively low rock quality in the ore zones. The mining method used is cut-and-fill. At current rates of production, more than 20 years of mining life is remaining in the considered mine. This demands good maintenance of tunnels and their ensured duty life. Besides of two shafts for ventilation, for men and materials transportation, and ore hoisting, development drifts were designed to extract and transport the ore. Figures 1 and 2 provide the plan view and vertical view of the drifts, respectively. It is a large and complex tunnel system with inclinations, curves and intersections. The volume inside the black square, shown in Fig. 1, is the selected part for stress analysis. The extent of this selected volume is given by E67900–E68100 and

N60000–N60200 on the horizontal plane with the elevation demarcations of 3075–3275 ft in the vertical direction.

The stratigraphy at this mine consists of carbonaceous mudstones and limestone, tuffaceous mudstones and limestone, polyolithic megaclastic debris flows, fine-grained debris flows and basalts, all part of the Cambrian-Ordovician Comus formation. These units are overlain by more basalts, mudstones and cherts that may be part of the Ordovician Valmy formation or may be a continuation of the Comus formation. The regional geology of the mine area is structurally and stratigraphically complex with intrusive dikes and sills. Most faults in this mine area are roughly striking NS or NW-SE with high dip angles. Faults with small offsets are observed commonly underground and it is difficult to trace most of the faults for more than a few hundred feet. In the selected area, a non-persistent fault exists. No in situ stress measurement has been conducted for this mine. The empirical relation for the in situ or virgin stresses with depth before mining has been estimated based on the work done in other mines and regional data. In the literature it is difficult or rare to find rock mass stability investigations conducted in underground mines in three dimensions using discontinuum numerical modeling techniques having complex geological conditions and complex excavation systems under both with and without rock support systems. Such a study is conducted in this paper.

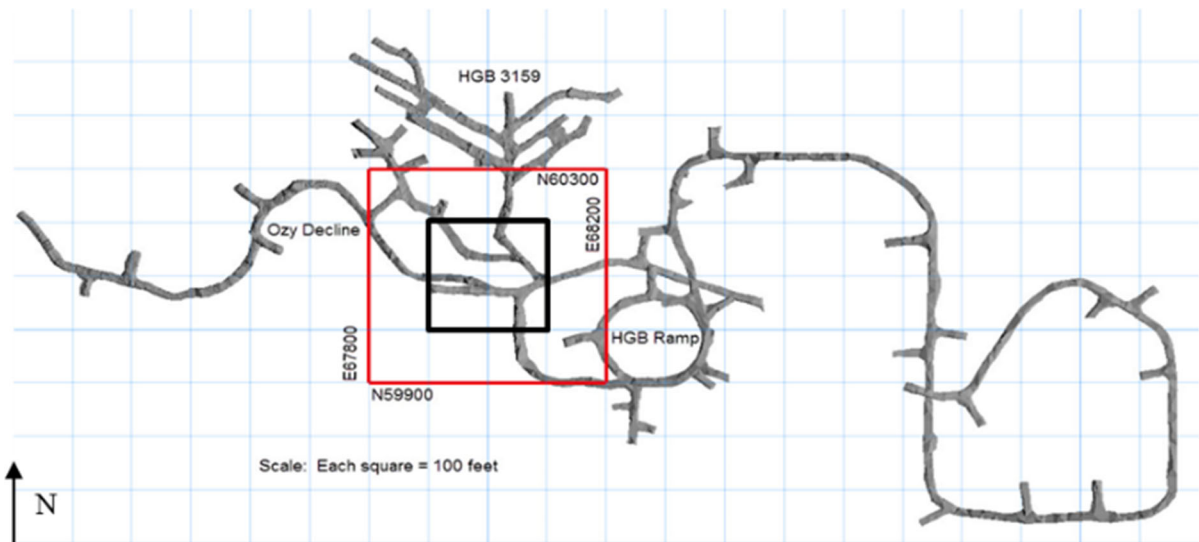


**Fig. 1** Plan view of the drifts (from the mining company)

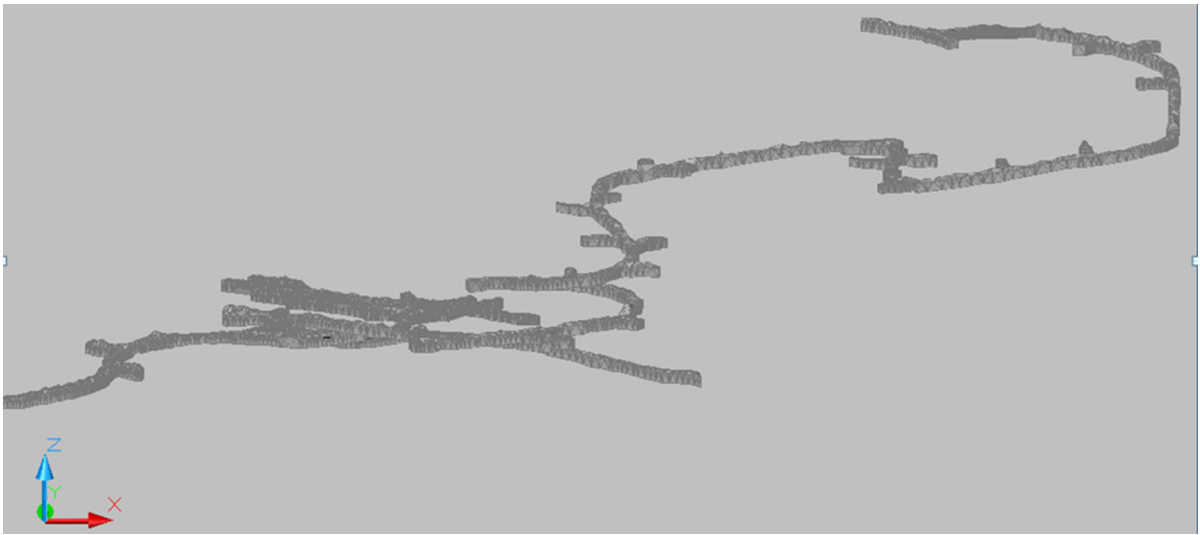


**Fig. 2** Vertical view of the drifts from south (from the mining company)

The purpose of this study is to thoroughly investigate the deformation and stability of the rock mass around selected tunnels in this mine under different conditions. A three-dimensional numerical model is set up using the three dimensional distinct element code (3DEC) (Itasca 2007) software package for performing stress analysis. First, because no in situ stress measurement is available, three different lateral stress ratios are assigned within a considerable range to study the effect of in situ stresses on stability. Secondly, two types of boundary conditions are applied to determine which one is more appropriate for simulating the in situ stress conditions in the field. In addition, to have a better understanding on how the post failure properties of rock masses can affect the stability around tunnels, both the Mohr–Coulomb and strain-softening models are applied and the results are compared. Cases with and without supports are evaluated to examine the effectiveness of supports, which offers a guidance to design more applicable support systems for the mining company. Finally, numerical predictions are compared with the field deformation measurements conducted around the tunnels.

## 2 Literature Review

Due to the presence of natural discontinuities in the rock masses with inherent uncertainties, variability of

rock mass mechanical properties and the complicated in situ conditions arising from complex geology, modeling of real world underground rock mass systems is very challenging. Performance of large-scale in situ experiments is very difficult, expensive and time consuming. Numerical modeling is an effective method to simulate field underground rock mass stability problems to provide fundamental information, insight, and guidelines even with limited geological and geotechnical data (Jing 2003).

Continuum approaches, including the finite element method (FEM), the finite difference method (FDM), and the boundary element method (BEM), have been commonly used in the rock mechanics problems. These methods treat the rock as a continuous material. Although the discontinuities can be included explicitly, the methods are most often applicable for the conditions where the material has microstructure with a length scale much smaller than that of the objects that are normally of interest (Cundall and Hart 1992). Therefore, for the rock masses with significant discontinuities where heterogeneity, anisotropy and inelasticity are dominated, the discontinuum methods are more appropriate to use. In discontinuum methods, the medium is considered as a system comprised of discrete bodies which are connected by contacts or interfaces. Different from continuum methods, the discrete element method allows for large displacements and/or rotations, reproduces block movements quite well and can recognize new contacts

automatically as the calculation progresses (Itasca 2007). The distinct element method (DEM) (Cundall 1971, 1988) is a powerful technique to perform stress analyses in blocky rock masses formed by discontinuities. In this method, the rock mass is modeled as an assemblage of rigid or deformable blocks. Discontinuities are considered as distinct boundary interactions between these blocks; joint behavior is prescribed for these interactions. Because of its explicit solution algorithm, matrices never being formed, the method can accommodate large displacements, rotations and complex constitutive behavior for both intact material and discontinuities. Universal Distinct Element Code (UDEC) (Cundall 1980) and 3DEC (Itasca 2007) are the two DEM codes, for 2-D and 3-D numerical modeling respectively, mainly used by researchers to investigate the stability of underground rock mass structures. Chryssanthakis et al. (1997) used the UDEC to study the effect of fiber reinforced shotcrete in a tunnel along with the optimal excavation sequence by analyzing the stresses and deformations around the excavations. In the study of Shen and Barton (1997), UDEC was used to perform numerical simulations for four cases with different joint spacing; the shape and size of disturbed zones around the tunnels in jointed rock masses were obtained for the analyses. Hao and Azzam (2005) carried out a parametric study using UDEC to assess the effects of some fault parameters on underground rock mass stability. Jiang et al. (2006) evaluated the effect of geometrical distribution of rock joints on the underground opening by applying different fractal dimensions to joint densities and orientations and obtaining the results of deformations and plastic zones around the tunnel using UDEC. Funatsu et al. (2008) investigated effect of ground supports and reinforcements on tunnel stability using UDEC. However, because the discontinuity geometry and the rock mass lithological geometry is really three-dimensional (3-D), to investigate deformability and stability in underground excavations, it is most appropriate to resort to a 3-D discontinuum, numerical stress analysis technique that has the capability of performing stress analysis of rock blocks having both persistent and non-persistent discontinuities. Multiple 3-D investigations on underground rock mass stability has been conducted by the following researches. Using the structural geology data obtained from 3-dimensional laser scanning as input data, Fekete and Diederichs (2013)

established a discontinuum model by 3DEC numerical code to evaluate the stability of tunnels in a blocky rock mass. Wang et al. (2012) constructed a three-dimensional discontinuous numerical model using 3DEC, through which the effect of discontinuities on deformations around the tunnel was investigated. Kulatilake et al. (2013) used 3DEC to conduct the stress analyses around a tunnel located under high in situ stress conditions in a Chinese underground coal mine. Shreedharan and Kulatilake (2016) performed stability studies on the tunnels with different shapes and support systems in a deep coal mine by using 3DEC distinct element code.

The Mohr–Coulomb criterion has been the most commonly used failure criterion in the elasto-plastic analysis of rock masses because of its simplicity (Lee and Pietruszczak 2008). However, because the non-linear behavior of strength parameters in the post-fail region is often observed both in the laboratory and in the field of underground engineering (Read and Hegemier 1984), the strain-softening model is more applicable to use in stability analysis of underground excavations. Jiang et al. (2001) discussed the effects of the mechanical properties of soft rocks on the loosening pressure of tunnels based on the strain-softening model. He and Cao (2008) used FLAC3D to study the stability of a large underground stope resulting from a series of excavations by considering the strain softening behavior of the rock material. Wang et al. (2011) used a new finite element implementation with a strain-softening constitutive model and investigated the depth of plastic zone around an underground power station.

### 3 Developed Numerical Model and Conducted Analyses

#### 3.1 Built Numerical Model for the Selected Region

In this paper, 3DEC Version 4.1 software package (Itasca 2007) was used to build the numerical model and perform stress analyses. The domain considered for the numerical model is a 61 m (200 ft) cube as shown in Fig. 3. It consists of three strata as shown with different colors in Fig. 3a with an approximate inclination of 35° of each stratum. In the numerical modeling conducted in this paper, discontinuity

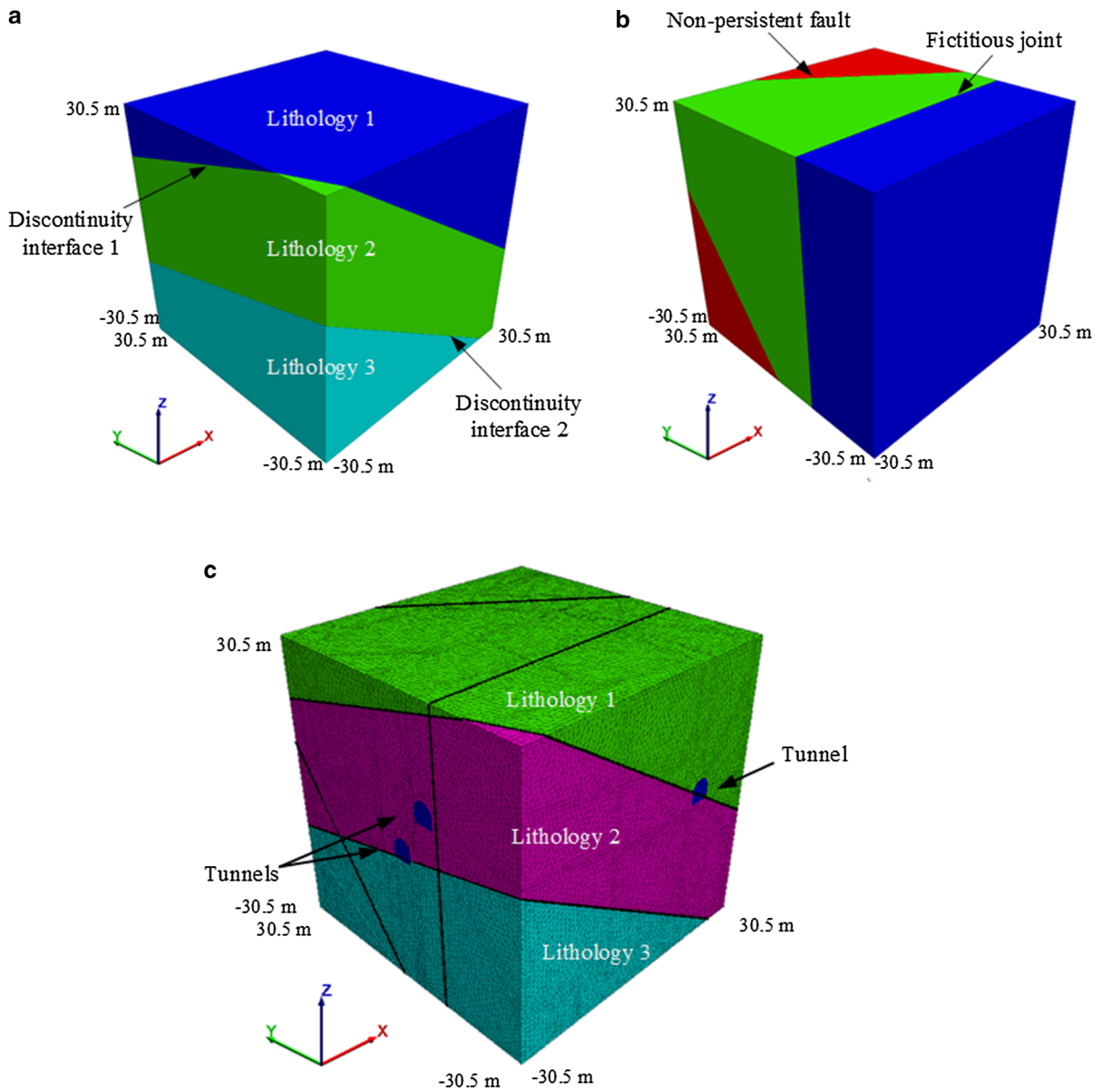


**Fig. 3** Generated block for the numerical model (61 m (200 ft) cube). **a** Lithology model. **b** Fault model. **c** Meshed model with all features

interfaces are included between two adjacent lithologies as shown in Fig. 3a. The simplified stratification is constructed based on the geologic profiles obtained from the mining company. A non-persistent fault dipping southwest is added to the model by generating a fictitious joint (see Fig. 3b). As far as the mechanical behavior is concerned, this fictitious joint should behave as intact material (Kulatilake et al. 1992, 1993). Figure 3c shows the meshed numerical

model generated with all the required features. Table 1 shows the orientations of the discontinuity interfaces and fault. The used coordinate system is shown in Fig. 3, and the point of  $x = 0, y = 0, z = 0$  is located at the center of the cube.

Figures 3c and 4 show the tunnels that exist in the studied area. All the tunnels are of horseshoe shape with a semicircular arch and the dimensions of the cross section are 15'W × 16'H (4.6 m × 4.9 m) as

shown in Fig. 5. As mentioned before, the tunnel system is complicated with inclinations and different heading directions. Good matches obtained between the Auto CAD and 3DEC models illustrated in Fig. 4 indicate that the tunnels built in the 3DEC model using the auto cad files are reliable.

### 3.2 Mechanical Properties for Lithologies and Discontinuities

The mechanical property values used to represent the rock masses in the numerical model (Table 2) were estimated based on the values of the rock mass rating

**Table 1** Orientations of the discontinuity interfaces and fault (also see Fig. 3a, b)

|                           | Dip angle (°) | Dip direction (°) |
|---------------------------|---------------|-------------------|
| Discontinuity interface 1 | 35.0          | 69.0              |
| Discontinuity interface 2 | 34.1          | 69.7              |
| Fault                     | 60.0          | 217.3             |

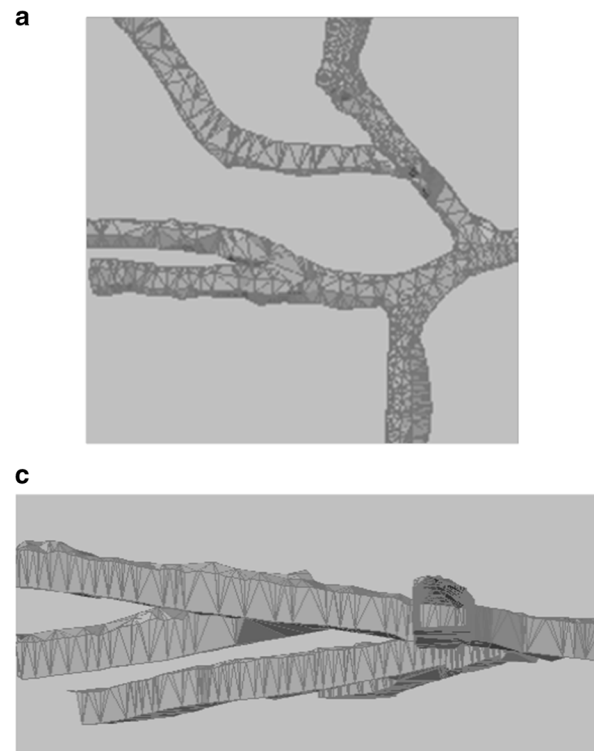


**Fig. 4** Tunnels that exist in the studied area. **a** Plan view of the tunnels from the Auto CAD file (from the mining company). **b** Plan view of the tunnels built in 3DEC. **c** Vertical view of the

(RMR) and the mechanical property values available from the mining company for the studied region. The selected mechanical property values represent the rock mass properties including the minor discontinuities, such as joints, fissures and fractures. Mechanical property values used for the fault, discontinuity interfaces and fictitious joints are shown in Table 3. The fault is considered to be closed and smooth with

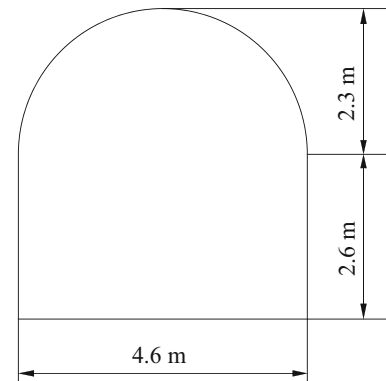
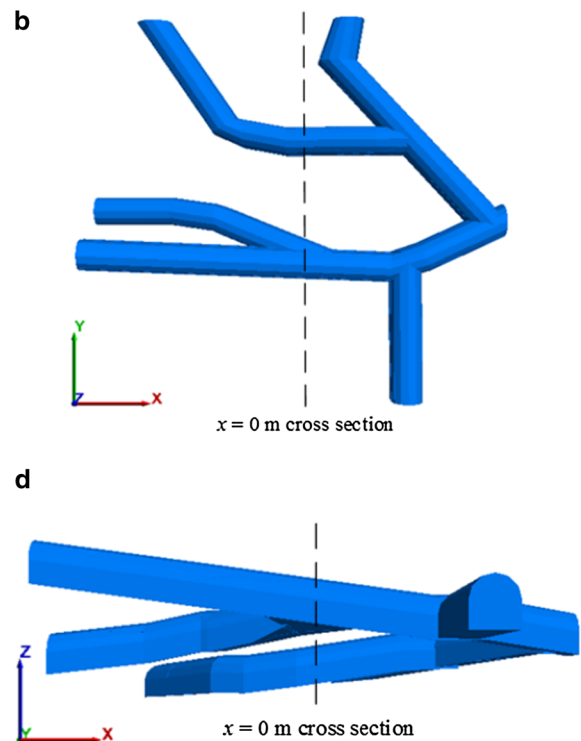


**Fig. 5** Dimensions of the tunnel cross section for all the tunnels



tunnels from the Auto CAD file (from the mining company). **d** Vertical view of the tunnels built in 3DEC

**Table 2** Mechanical property values used to represent the rock mass for different lithologies

| Lithology (see Fig. 3a) | Density (kg/m <sup>3</sup> ) | Elastic modulus (GPa) | Poisson's ratio | Uniaxial compressive strength (MPa) | Cohesion (MPa) | Friction angle (°) | Tensile strength (MPa) |
|-------------------------|------------------------------|-----------------------|-----------------|-------------------------------------|----------------|--------------------|------------------------|
| 1                       | 2600                         | 15.08                 | 0.25            | 31.63                               | 8.55           | 33.2               | 2.25                   |
| 2                       | 2600                         | 2.58                  | 0.27            | 16.72                               | 4.72           | 31.1               | 1.50                   |
| 3                       | 2600                         | 15.08                 | 0.25            | 31.63                               | 8.55           | 33.2               | 2.25                   |

**Table 3** Mechanical property values used for discontinuities

| Discontinuity type (see Fig. 3)       | Friction angle (°) | Cohesion (MPa) | Tensile strength (MPa) | Normal stiffness (GPa/m) | Shear stiffness (GPa/m) |
|---------------------------------------|--------------------|----------------|------------------------|--------------------------|-------------------------|
| Fault                                 | 25.0               | 0              | 0                      | 5                        | 1                       |
| Interface between lithologies 1 and 2 | 32.2               | 6.63           | 1.87                   | 1099.2                   | 439.7                   |
| Interface between lithologies 2 and 3 | 32.2               | 6.63           | 1.87                   | 1099.2                   | 439.7                   |
| Fictitious joint in lithology 1       | 33.2               | 8.55           | 2.25                   | 1882.2                   | 752.9                   |
| Fictitious joint in lithology 2       | 31.1               | 4.72           | 1.50                   | 316.3                    | 126.5                   |
| Fictitious joint in lithology 3       | 33.2               | 8.55           | 2.25                   | 1882.2                   | 752.9                   |

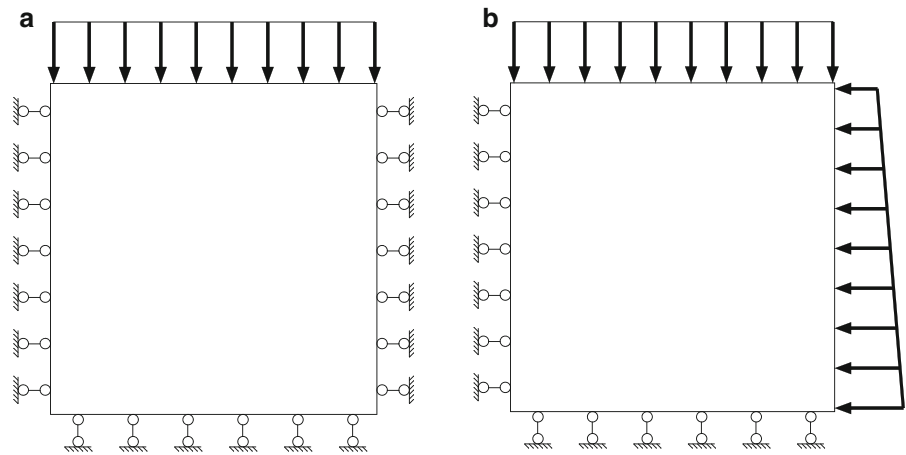
no filling material. Accordingly, a zero value is assigned for the cohesion and tensile strength of the fault. The mechanical property values of fictitious joints were estimated using the method suggested by Kulatilake et al. (1992). In this paper, the joint shear stiffnesses (JKS) of the fictitious joints were estimated using the expression shear modulus/JKS ratio = 0.008. The joint normal stiffnesses (JKN) were estimated using the expression JKN/JKS ratio = 2.5. The same strength parameter values were assigned for both the rock mass and fictitious joints. The mechanical property values of interfaces were estimated by first calculating the average values between the two materials and then using the aforementioned method suggested by Kulatilake et al. (1992). The discontinuity interfaces were considered as well-bonded interfaces between the two adjacent lithologies rather than as weakness planes. Therefore, as far as the mechanical behavior is concerned, they should represent a gradual transition between the two materials. Hence, the average properties of the two lithologies, which can simulate the gradual variation, were used to estimate the corresponding interface properties following the same procedures as for the fictitious joints.

### 3.3 Boundary Conditions and In-situ Stresses

Because of the influences of the inclined lithologies and the existing fault, it is difficult to estimate the in situ stresses either through field measurements or through analytical calculations and apply in situ stresses in the numerical model. The proper way to obtain the in situ stresses for complicated geological systems is to apply appropriate boundary stresses and to perform numerical modeling as given in Tan et al. (2014a, b).

The top boundary of the model is located at a depth range of 590–680 m. A vertical stress of 14 MPa was applied at the top of the model to simulate the gravitational loading of the overburden strata. This is based on an average overburden depth of 635 m and an overburden material density of 2250 kg/m<sup>3</sup>. The Roller boundary condition was used at the bottom boundary (no displacement or velocity is allowed in the vertical direction). For lateral boundaries, two kinds of conditions were specified. First, the roller boundaries are applied in the x- and y-directions as shown in Fig. 6a (no horizontal displacement or velocity is allowed in the two directions). Due to the asymmetry of faults, lithologies, and tunnels, stress

**Fig. 6** Boundary conditions applied in the numerical model. **a** Velocity boundaries. **b** Mixed boundaries



boundaries cannot be applied at all the four lateral boundaries. If it is implemented, the numerical model will keep moving and rotating without attaining the equilibrium. Thus, the roller boundary condition was applied on one side and the stress boundary condition was applied on the other side in both horizontal directions as shown in Fig. 6b. Note that the boundary condition system applied in Fig. 6b is termed as the mixed boundary condition in this paper. On the stress boundaries, the vertical stress was increased from the top to bottom of the model according to the gravitational loading. The values of 0.5, 1.0, and 1.5 were assigned to the lateral stress ratio to obtain three different horizontal stress systems according to the same vertical stress system (assuming the same  $K_0$  values in the x- and y-directions). The mixed boundary condition was used in the following analyses.

### 3.4 Material Constitutive Model

3DEC has five built-in material models for deformable blocks. In this paper, the Mohr–Coulomb model and strain-softening model were used.

The Mohr–Coulomb model is the conventional model used to represent shear failure in soils and rocks. In this model, the mechanical behavior of deformable blocks is represented by a linear-elastic, perfectly plastic constitutive model with the Mohr–Coulomb failure criterion ( $f_s = 0$ ), including a tension cutoff ( $f_t = 0$ ). The expressions of  $f_s$  and  $f_t$  are given by (Itasca 2007)

$$f_s = \sigma_1 - \sigma_3 N_\phi + 2c\sqrt{N_\phi} \quad (1)$$

$$f_t = \sigma_3 - \sigma^t \quad (2)$$

where  $\sigma_1$  is the major principal stress,  $\sigma_3$  is the minor principal stress,  $\phi$  is the friction angle,  $c$  is the cohesion,  $\sigma^t$  is the tensile strength, and

$$N_\phi = (1 + \sin \phi)/(1 - \sin \phi) \quad (3)$$

The shear failure is detected if  $f_s < 0$  and the tensile failure occurs when  $f_t > 0$ .

In 3DEC, for the Mohr–Coulomb model, the strength properties of the material are assumed to remain constant after the onset of plastic failure. Therefore, it is recommended to be applied for the problems where the post failure response of the materials is less important. The typical stress–strain curve for the elastic–perfectly plastic model is shown in Fig. 7.

The strain-softening model (Fig. 8) is an extended constitutive model based on the Mohr–Coulomb model. It allows representation of nonlinear material softening behavior of the strength properties (cohesion, friction, dilation, tensile strength) as functions of the plastic portion of the total strain.

The increments of plastic shear and tensile strain parameters ( $\Delta \epsilon^{ps}$ ,  $\Delta \epsilon^{pt}$ ) used to define the strength properties can be calculated by Eqs. (4) and (5), respectively (Itasca 2007).

$$\Delta \epsilon^{ps} = \frac{1}{\sqrt{2}} \sqrt{(\Delta \epsilon_1^{ps} - \Delta \epsilon_m^{ps})^2 + (\Delta \epsilon_m^{ps})^2 + (\Delta \epsilon_3^{ps} - \Delta \epsilon_m^{ps})^2} \quad (4)$$

$$\Delta \epsilon^{pt} = |\Delta \epsilon_3^{pt}| \quad (5)$$



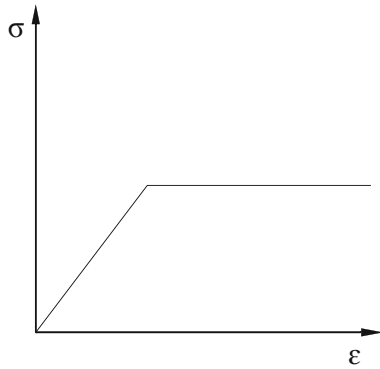


**Fig. 7** Typical stress–strain curve of the Mohr–Coulomb model

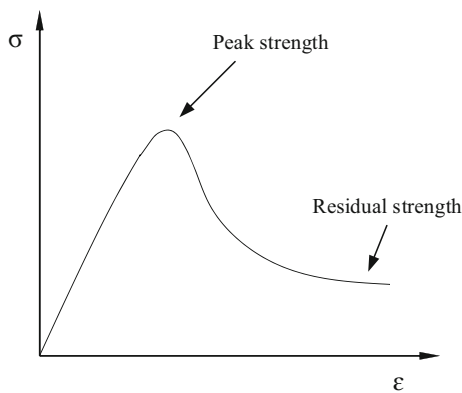


**Fig. 8** Stress–strain curve of the strain-softening model

In Eq. (4),  $\Delta\epsilon_m^{ps}$  is the volumetric plastic shear strain increment given by Eq. (6),

$$\Delta\epsilon_m^{ps} = \frac{1}{3} (\Delta\epsilon_1^{ps} + \Delta\epsilon_3^{ps}) \tag{6}$$

and the plastic strain increments  $\Delta\epsilon_1^{ps}$ ,  $\Delta\epsilon_3^{ps}$ , and  $\Delta\epsilon_3^{pt}$ , given in Eqs. (4) and (5), can be obtained based on the flow rule.

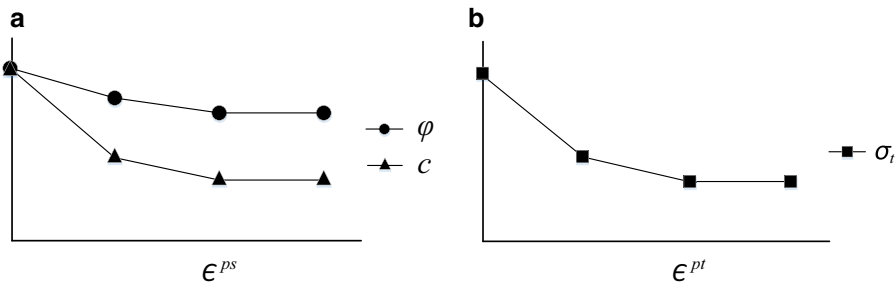


**Fig. 9** Conceptual variation of cohesion, friction angle, and tensile strength with plastic strain parameters: **a** cohesion and friction angle. **b** Tensile strength

The relations between strength properties and  $\epsilon^{ps}$ ,  $\epsilon^{pt}$  can be approximated as sets of linear segments as shown in Fig. 9 (Itasca 2007).

For the applications where the post-failure response is important and the plastic strain is required, the strain-softening model is recommended. In this research, the friction angle was kept constant and the cohesion was reduced as a function of the plastic shear strain parameter. Because there is no available laboratory data about cohesion degradation of the rock types used in this research, the results from some references (Hajiabdolmajid et al. 2002; Ray 2009; Wang et al. 2011) were reviewed and utilized (Fig. 10). A similar relation was defined between the tensile strength and the plastic tensile strain parameter.

With respect to the fault, discontinuity interfaces, and fictitious joints, a joint area contact Coulomb slip model was applied in this study. The model provides a linear representation of the joint stiffness and yield limit, and is based on the elastic stiffness, frictional, cohesive and tensile strength properties, and dilation characteristics common to rock joints. The model simulates displacement-weakening of the joint by loss

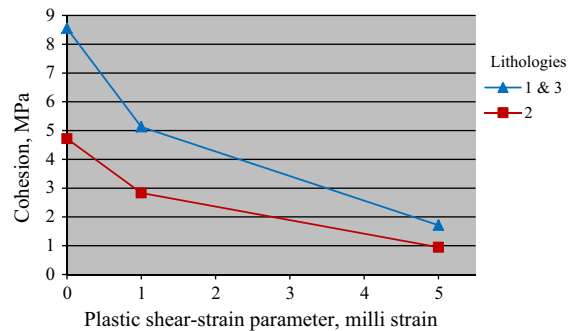


**Fig. 10** Used degradation of cohesion for different lithologies

of cohesive and tensile strength at the onset of shear or tensile failure (Itasca 2007).

### 3.5 Support System

Both rock bolts and cable bolts have been used for ground control in this mine. The cross sections given in Fig. 11 show the rock bolt patterns used for all the tunnels. The roof bolts have two patterns which are respectively three bolts (Fig. 11a) and four bolts (Fig. 11b) at each cross section. These two rock bolt patterns alternate along the tunnel axis. The length of the bolts is 2.44 m; the spacing between adjacent bolts in the cross sectional plane is 1.2 m. Besides, in each cross sectional plane, there are 8 rib bolts of length 1.83 m; the lowest bolts in the walls are 0.9 m high above the floor. The spacing between the adjacent bolts along the tunnel axis is approximately 1.2 m. The bolts have been installed perpendicular to the tunnel surface. Additional 6.1 m cable bolts have been applied in the roof for part of the tunnels (the part shown in red and labeled in Fig. 12). Two patterns of cable bolts (Fig. 13) have been installed along the tunnel axis. The spacing of adjacent bolts on and perpendicular to the tunnel cross sectional plane is 1.8 m. Cable bolts have been placed in between rock bolts along the tunnel axis. Table 4 shows the parameter values used to represent cables/bolts in the numerical model. They were estimated based on the information provided by the mining company and the

equations available in the Itasca manual. The used equations are given as follows (Itasca 2007).

The grout shear stiffness per cable length can be estimated by

$$K_{bond} = \frac{2\pi G}{10 \ln(1 + 2t/D)} \quad (7)$$

where  $G$  is the grout shear modulus,  $D$  is the reinforcement diameter, and  $t$  is the annulus thickness.

The grout cohesive capacity per cable length can be estimated by

$$S_{bond} = \pi(D + 2t)\tau_{peak} \quad (8)$$

where  $\tau_{peak}$  is the peak shear strength of the grout.

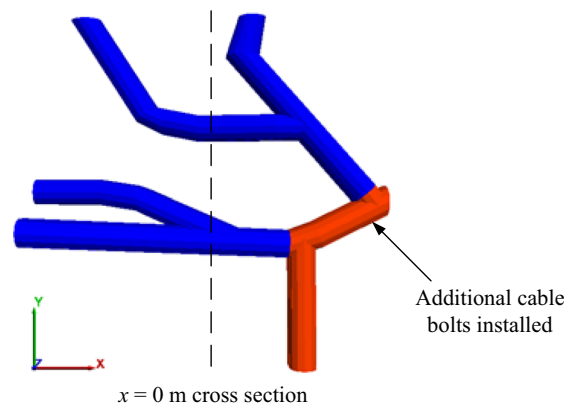


**Fig. 12** Diagram of the part of the tunnels with additional cable bolts

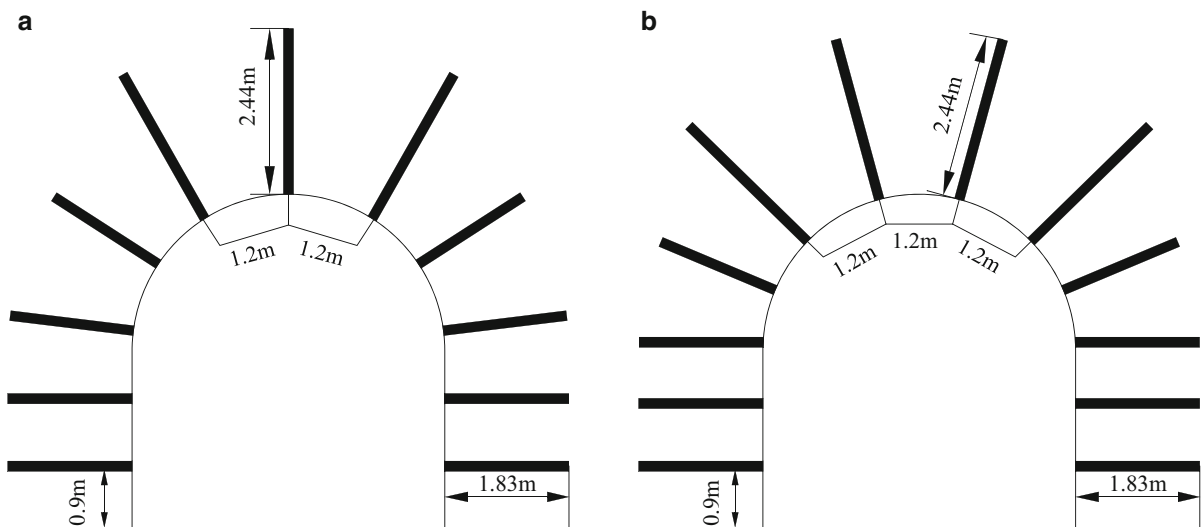


**Fig. 11** Diagram of the tunnel cross section with rock bolts

**Fig. 13** Diagram of the tunnel cross section with additional cable bolts

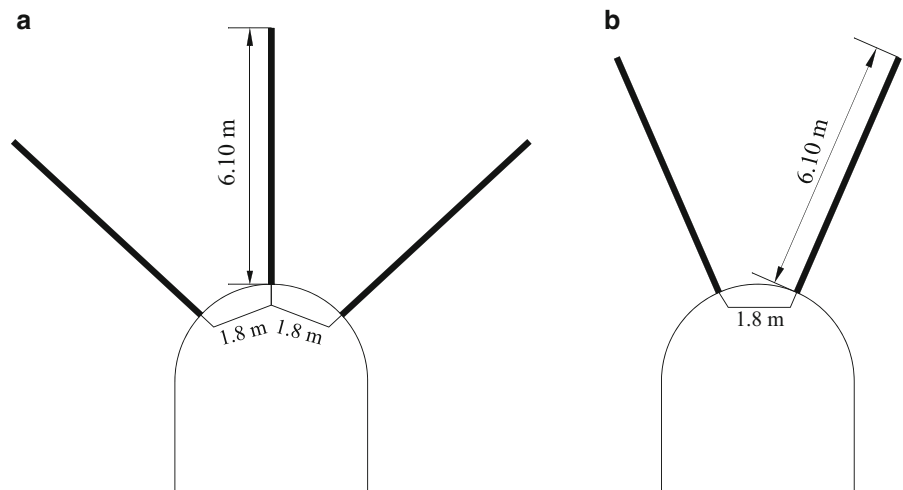


**Table 4** Parameter values used to represent cable/bolt structure in the numerical model

| Type of support (see Figs. 11, 12, 13) | Young’s modulus (GPa) | Cross-sectional area (m <sup>2</sup> ) | Tensile yield capacity of the bolt (KN) | Grout cohesive capacity per unit length (KN/m) | Grout stiffness per unit length (MN/m/m) |
|--|-----------------------|--|---|--|--|
| Rock bolts (roof)                      | 200                   | $3.80 \times 10^{-4}$                  | 160                                     | $1.0 \times 10^3$                              | $6.5 \times 10^3$                        |
| Rock bolts (wall)                      | 200                   | $1.20 \times 10^{-3}$                  | 120                                     | 500  | $1.0 \times 10^3$                        |
| Cable support                          | 200                   | $1.27 \times 10^{-4}$                  | 160                                     | $1.0 \times 10^3$                              | $6.5 \times 10^3$                        |

### 3.6 Conducted Analyses

The different numerical stress analyses performed in this paper are summarized in Table 5. Nine cases are considered with different boundary conditions,  $K_0$  values, material constitutive models and support systems.

## 4 Discussion of Results

### 4.1 Checking of the Basic Numerical Model Results

Before analyzing the effect of several factors on the stability and deformation around the tunnels, the basic numerical model was checked using case 3 (see Table 5) results as given in the next paragraph.

Figure 14a, b show the distributions of zz-stress and yy-stress, respectively obtained around the tunnels. The vertical stress at the top boundary is

not affected by the excavations and it agrees with the specified boundary stress. Zero stress occurs on the roof as well as on the floor of the tunnels; it means that the tunnel excavation has caused stress relief, which is intuitively expected. In addition, the maximum zz-stress takes place adjacent to the walls of the tunnels (see Fig. 14a). With respect to the yy-stress (shown in Fig. 14b), the stresses at the lateral boundaries match with the applied boundary conditions. Zero values appear at the walls of the tunnels. Figure 15 shows the principal stress vectors obtained around the tunnels. The vectors illustrate that the stress perpendicular to the excavation surfaces reaches zero; this agrees with the intuition. The stress magnitudes agree well with the stress states in Fig. 14. Also it can be seen that the directions of the principal stresses inside the model are not simple and uniform and they are affected by the fault and inclined strata. In summary, all these results show that the numerical model behaves correctly under the applied inputs.

**Table 5** Summary of the performed stress analyses cases

|        | Boundary condition | $K_0$ value | Material constitutive model | Support system included or not |
|--------|--------------------|-------------|-----------------------------|--------------------------------|
| Case 1 | R <sup>a</sup>     | –           | M–C <sup>c</sup>            | No                             |
| Case 2 | M <sup>b</sup>     | 0.4         | M–C <sup>c</sup>            | No                             |
| Case 3 | M <sup>b</sup>     | 0.5         | M–C <sup>c</sup>            | No                             |
| Case 4 | M <sup>b</sup>     | 1.0         | M–C <sup>c</sup>            | No                             |
| Case 5 | M <sup>b</sup>     | 1.5         | M–C <sup>c</sup>            | No                             |
| Case 6 | M <sup>b</sup>     | 0.5         | s–s <sup>d</sup>            | No                             |
| Case 7 | M <sup>b</sup>     | 1.0         | s–s <sup>d</sup>            | No                             |
| Case 8 | M <sup>b</sup>     | 1.5         | s–s <sup>d</sup>            | No                             |
| Case 9 | M <sup>b</sup>     | 1.0         | s–s <sup>d</sup>            | Yes                            |

<sup>a</sup> R stands for roller (velocity) boundary condition (see Fig. 6a)

<sup>b</sup> M stands for mixed boundary condition (see Fig. 6b)

<sup>c</sup> M–C stands for Mohr–Coulomb model

<sup>d</sup> s–s stands for strain-softening model

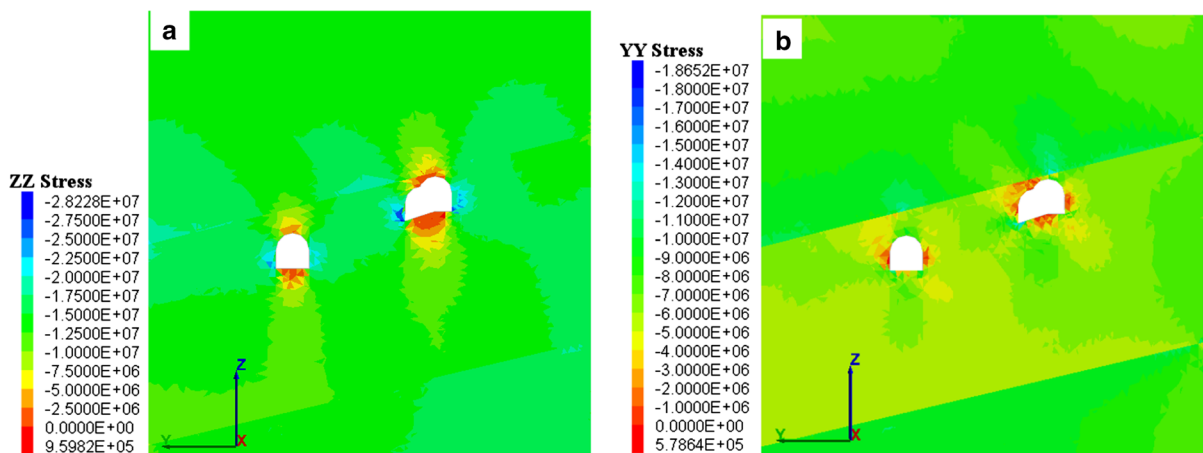


**Fig. 14** Stress distributions around the tunnels for case 3 ( $K_0 = 0.5$ ) at the vertical cross section  $x = 0$  m (unit: Pa). **a** zz-stress distribution. **b** yy-stress distribution

#### 4.2 Effect of $K_0$ on the Deformation and Stability Around the Tunnels

As discussed above, the in situ stress is not easy to calculate analytically and apply in the considered mine problem, and it is necessary to obtain it through numerical stress analysis by applying proper boundary conditions. Therefore, in order to study the effect of in situ stress on stability around the tunnels, different boundary stresses were applied by using  $K_0$  values of 0.5, 1.0, and 1.5, while having the same vertical stress system.

Figures 16 and 17 show respectively the distributions of z-displacement and y-displacement obtained for cases 3, 4, and 5 with the same color legend. The maximum displacement values around the tunnels for different cases are given in Table 6. Results show that the maximum z-displacements on the roof and floor of the tunnels decrease with the increase of  $K_0$ . Case 3 has the highest maximum values, which are respectively 23.3 mm on the roof and 42.0 mm on the floor. Note that the material above the roof is mainly lithology 1. On the other hand, the material below the floor is mainly lithology 2, which is significantly softer

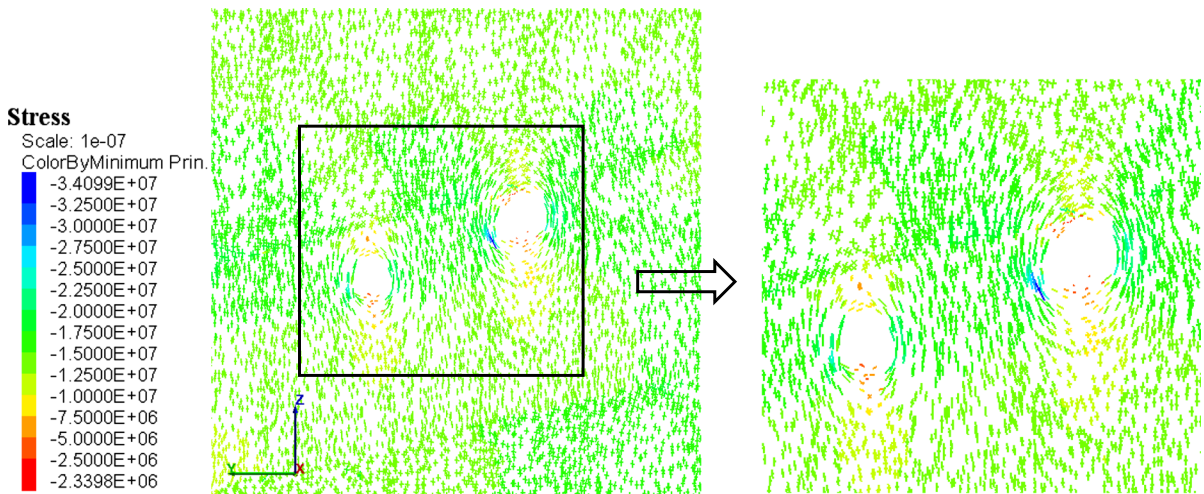


**Fig. 15** Principal stress vector distribution around the tunnels for case 3 ( $K_0 = 0.5$ ) at the vertical cross section  $x = 0$  m (unit: Pa)

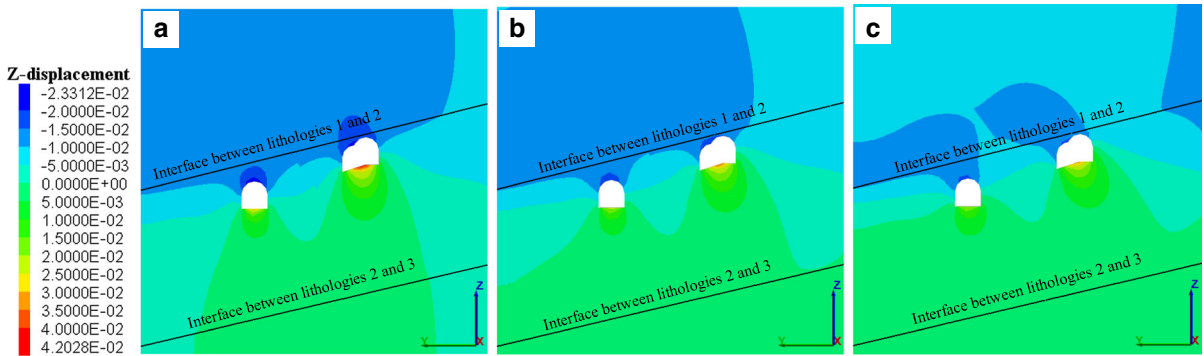


**Fig. 16** Z-displacement distributions around the tunnels for different  $K_0$  values at the vertical cross section  $x = 0$  m (unit: m). **a** Case 3 ( $K_0 = 0.5$ ). **b** Case 4 ( $K_0 = 1.0$ ). **c** Case 5 ( $K_0 = 1.5$ )

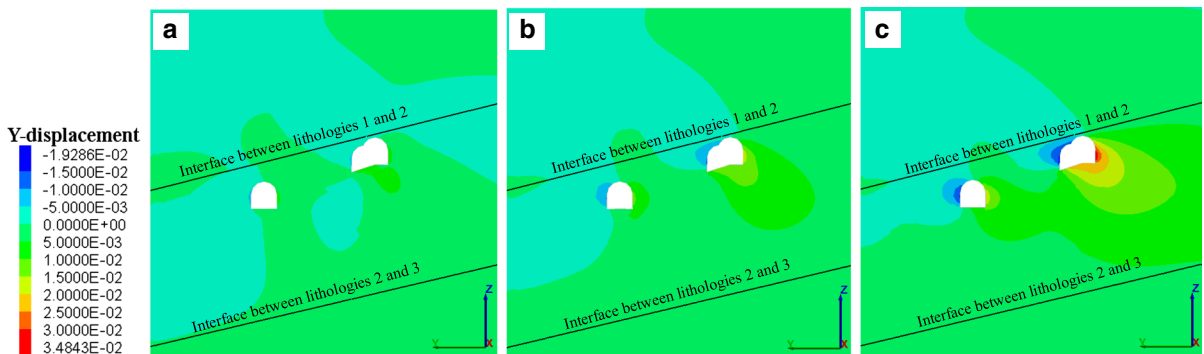


**Fig. 17** Y-displacement distributions around the tunnels for different  $K_0$  values at the vertical cross section  $x = 0$  m (unit: m). **a** Case 3 ( $K_0 = 0.5$ ). **b** Case 4 ( $K_0 = 1.0$ ). **c** Case 5 ( $K_0 = 1.5$ )

than lithology 1. This is the main reason for floor deformations to be higher than the roof deformations. The maximum y-displacement on the walls of the

tunnels increases with the  $K_0$ . The values increased from 6.9 to 19.3 mm on the left wall and from 10.0 to 34.8 mm on the right wall with increasing  $K_0$ .

**Table 6** Effect of  $K_0$  on the deformation and failure zone around tunnels

|                        | Max. z-disp. value on floor (mm) | Max. z-disp. value on roof (mm) | Max. y-disp. value on walls (mm) | Max. dist. of failure zone on floor (m) | Max. dist. of failure zone on roof (m) | Max. dist. of failure zone on walls (m) |
|------------------------|----------------------------------|---------------------------------|----------------------------------|---|--|---|
| Case 3 ( $K_0 = 0.5$ ) | 42.0                             | 23.3                            | 10.0                             | 2.44                                    | 2.35                                   | 1.75                                    |
| Case 4 ( $K_0 = 1.0$ ) | 33.7                             | 19.4                            | 19.7                             | 1.64                                    | 2.33                                   | 1.52                                    |
| Case 5 $K_0 = 1.5$     | 31.1                             | 17.2                            | 34.8                             | 2.03                                    | 3.23                                   | 1.78                                    |

The failure zones and the maximum failure distances obtained around the tunnels for the three cases are given in Fig. 18 and Table 6. Case 5 ( $K_0 = 1.5$ ) has the maximum number of failure elements around the tunnels. The maximum failure distances on the roof, floor and walls of the tunnels are respectively 3.23, 2.03, and 1.78 m. For case 5, the main failure type appearing on the walls is shear failure; on the roof and floor both shear and tensile failure types have taken place. For cases 3 ( $K_0 = 0.5$ ) and 4 ( $K_0 = 1.0$ ), the roof and floor are dominated by the tensile failure; shear failure has taken place on the walls. The main difference between the cases 3 and 4 is that case 3 has more failure elements on the roof and floor than case 4. Therefore, case 5 ( $K_0 = 1.5$ ) is the most unstable and case 4 ( $K_0 = 1.0$ ) is the least unstable.

#### 4.3 Effect of Material Constitutive Models on the Deformation and Stability Around the Tunnels

Cases 4 (M–C) and 7 (s–s) are considered in this section to investigate the effect of different constitutive models on the failure condition and stability around the tunnels. First, comparison of the results is

shown between the Mohr–Coulomb model and strain-softening model. Then a new method to evaluate the failed elements around the tunnels is suggested. In the strain-softening model, because the strength of the material reduces as a function of the plastic shear strain rather than staying constant at the post failure stage as in the standard Mohr–Coulomb model, the numerical model would obviously suffer more deformation and failure around the excavations.

Figures 19, 20 and 21 show the distributions of displacement and failure zone status around the tunnels for the Mohr–Coulomb and strain-softening models. Table 7 shows the maximum displacements and maximum failure distances around the tunnels. Results show that both the z-displacement and y-displacement have increased significantly when the post failure softening of the rock masses is considered. The maximum z-displacement on the roof increased from 19.4 to 31.1 mm and the maximum displacement on the floor increased from 33.7 to 40.6 mm. At the same time, the maximum y-displacement on the walls increased from 19.7 to 43.5 mm (Table 7). Obvious changes of failure zones around the tunnels have taken place on the walls; case 7 has more shear failure elements than case 4 (see Fig. 21). This can be verified

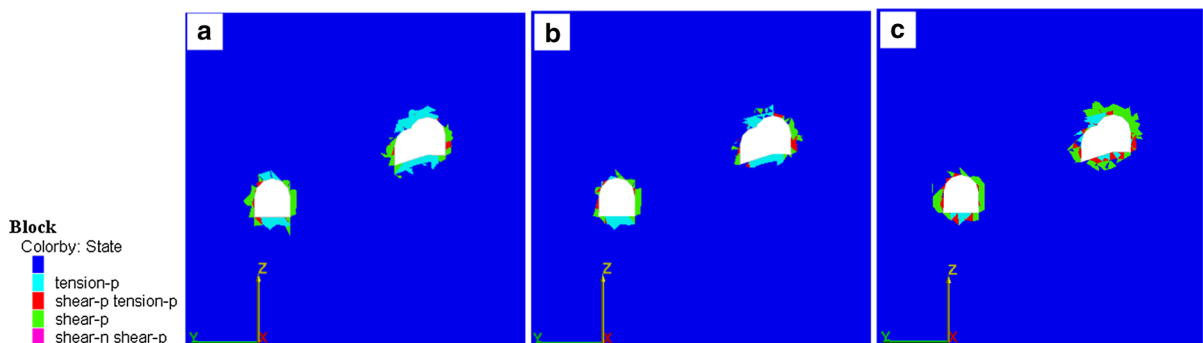


**Fig. 18** Failure zone distributions around the tunnels for different  $K_0$  values at the vertical cross section  $x = 0$  m. **a** Case 3 ( $K_0 = 0.5$ ). **b** Case 4 ( $K_0 = 1.0$ ). **c** Case 5 ( $K_0 = 1.5$ )

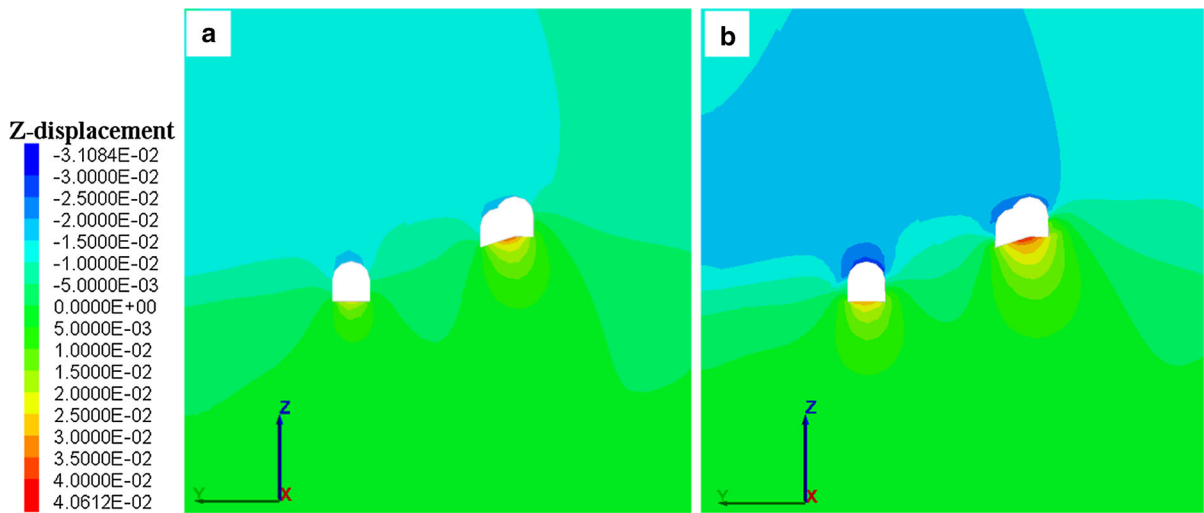


**Fig. 19** Z-displacement distributions for the two constitutive models at the vertical cross section  $x = 0$  m (unit: m). **a** Case 4 (M–C). **b** Case 7 (s–s)

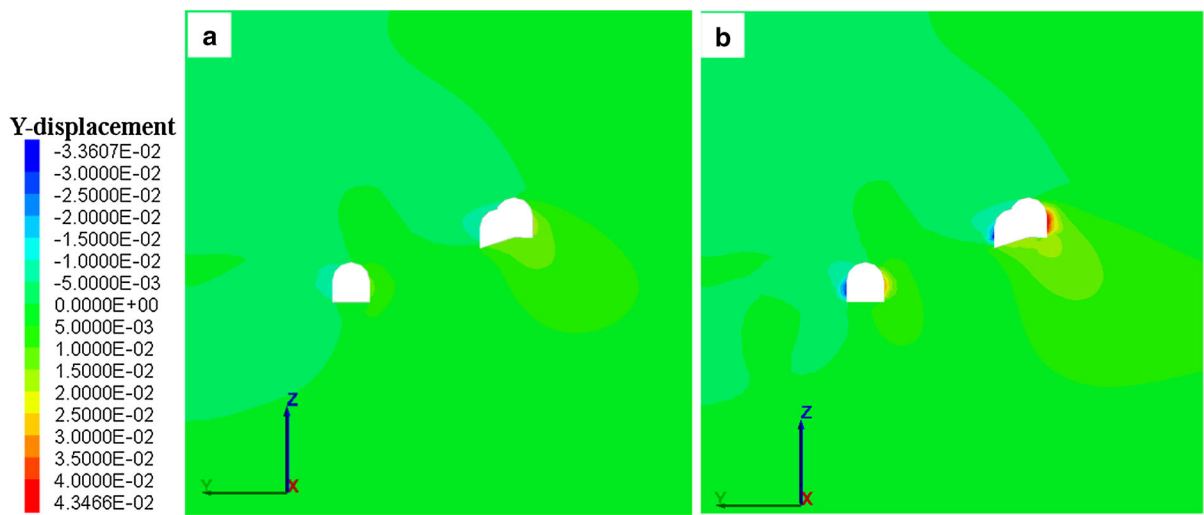


**Fig. 20** Y-displacement distributions for the two constitutive models at the vertical cross section  $x = 0$  m (unit: m). **a** Case 4 (M–C). **b** Case 7 (s–s)

by the increase of the maximum failure distances on the walls from 1.52 to 2.62 m. All the plots for comparisons are given with the same color legend to make accurate comparisons.

In the strain-softening model, the rock mass exhibits a progressive loss of strength when it is compressed beyond failure; the strength is progressively reduced until a generally low residual value is obtained. In 3DEC, the plastic indicator is a way used to assess the failure state of the numerical model for a

static analysis (Itasca 2007). It indicates that the plastic flow is occurring in those zones where the stresses exceed the yield criterion; and a failure mechanism is indicated for the zones. However, the strain softening behavior of the rock mass implies that the material still have the ability to support load after the onset of the plastic failure. Therefore, the unstable elements denoted by the plastic indicators do not properly represent the failed area. Therefore, in Fig. 21b the failed area around the tunnels is

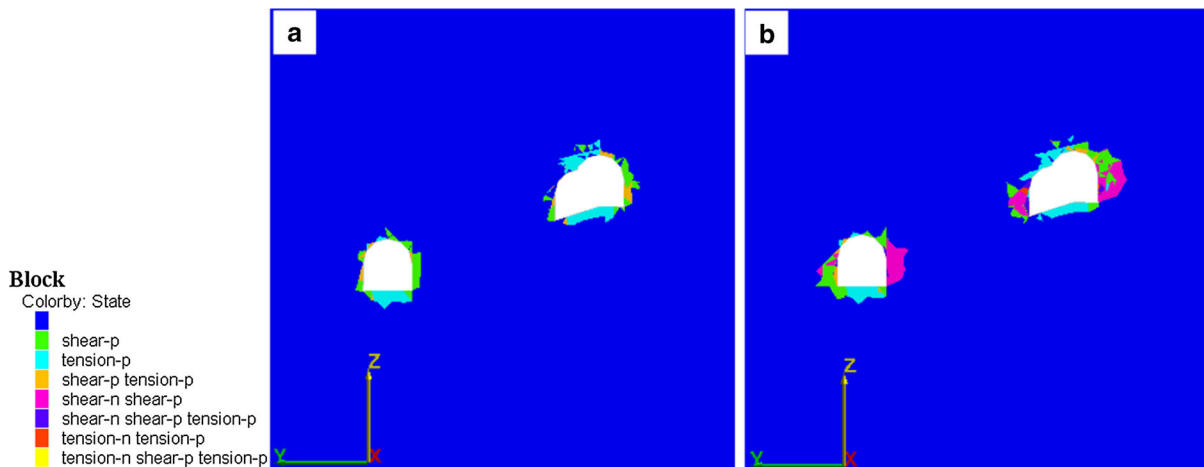


**Fig. 21** Failure zone distributions for the two constitutive models at the vertical cross section  $x = 0$  m. **a** Case 4 (M–C). **b** Case 7 (s–s)

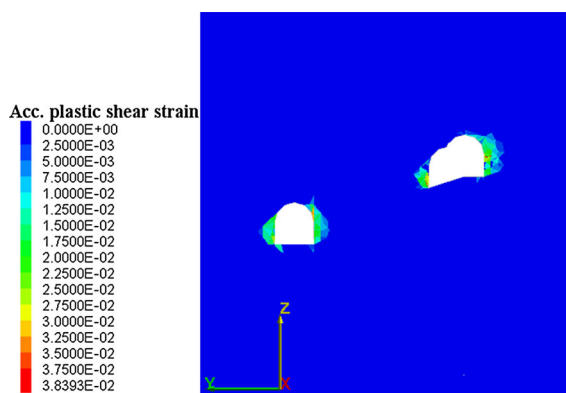
**Table 7** Effect of material constitutive models on the deformation and failure zone around tunnels

|              | Max. z-disp. value on floor (mm) | Max. z-disp. value on roof (mm) | Max. y-disp. value on walls (mm) | Max. dist. of failure zone on floor (m) | Max. dist. of failure zone on roof (m) | Max. dist. of failure zone on walls (m) |
|--------------|----------------------------------|---------------------------------|----------------------------------|---|--|---|
| Case 4 (M–C) | 33.7                             | 19.4                            | 19.7                             | 1.61                                    | 2.29                                   | 1.52                                    |
| Case 7 (s–s) | 40.6                             | 31.1                            | 43.5                             | 1.63                                    | 2.33                                   | 2.62                                    |

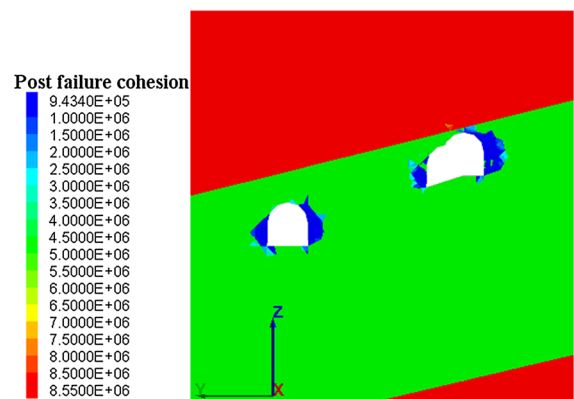
overestimated. In this research, the accumulated plastic shear strain as well as residual cohesion distributions are used to provide a better evaluation of the failed rock mass around the tunnels.

Figure 22 shows the accumulated plastic shear strain distribution around the tunnels for case 7. Most

of the plastic shear strain occurs at the walls of the tunnels with the maximum value around 3.84 %. It demonstrates the condition shown in Fig. 21b that most of the shear failure happens at the walls. Figure 23 is the post failure cohesion distribution around the tunnels. The degradation of cohesion



**Fig. 22** Accumulated plastic shear strain distribution around the tunnels for case 7 (s–s model) at the vertical cross section  $x = 0$  m



**Fig. 23** Post failure cohesion distribution around the tunnels for case 7 (s–s model) at the vertical cross section  $x = 0$  m (unit: Pa)



around the tunnels depicted in this plot coincides with the accumulated plastic shear strain distribution shown in Fig. 22. The darkest blue regions (residual cohesion value) appearing in Fig. 23 can be considered as the failed regions. It can be observed that this failed region determined by the residual cohesion value is smaller than the shear failure zones presented directly by the 3DEC in Fig. 21b according to the shear failure criterion.

#### 4.4 Effect of Different Boundary Conditions on the Deformation and Stability Around the Tunnels

The results of roller and mixed boundaries are compared in this part of the paper for cases 1, 2, and 3, and then the connection and differences among the three cases are discussed. All the plots are given with the same color legend to make accurate comparisons.

Comparisons of the distributions of zz-stress around the tunnels for the three cases are shown in Fig. 24. Results show that case 1 and case 2 have similar stress distributions not only in the shape but also in the magnitude. Similar findings appear for the yy-stress distributions shown in Fig. 25. All these findings indicate that the stress state appearing in the model by applying the roller boundaries is nearly the same as the stress state appearing in the model by applying stress boundaries with the  $K_0$  value of 0.4. Actually, for the roller boundary condition, the lateral stress ratio,  $\sigma_h/\sigma_v$  (horizontal stress/vertical stress) at the boundaries, can be calculated approximately by  $\nu/(1 - \nu)$  (where  $\nu$  is the Poisson’s ratio). In the numerical simulation of this paper, the values of 0.25 and 0.27 were assigned to the Poisson’s ratio of the rock masses as shown in Table 2. Therefore, the range of lateral stress ratio is between 0.33 and 0.37, which is close to 0.4. Note that the aforesaid calculation is strictly applicable for a medium with

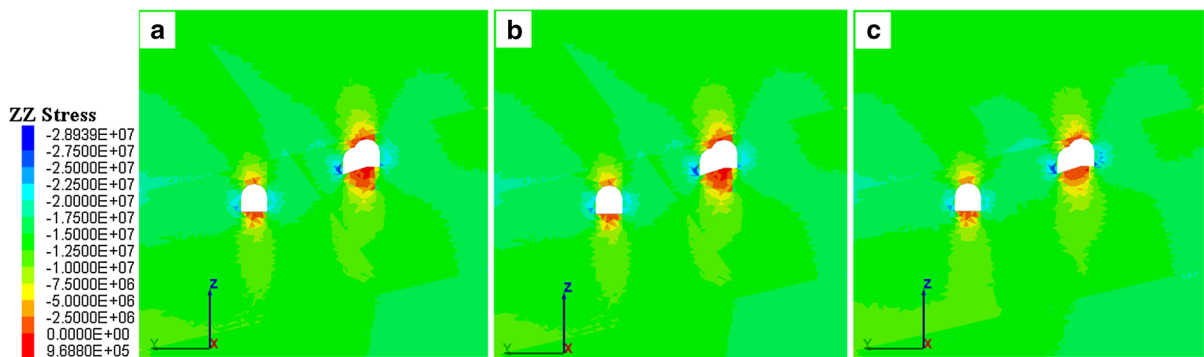


**Fig. 24** zz-stress distributions around the tunnels for different boundary conditions at the vertical cross section  $x = 0$  m (unit: Pa). **a** Case 1. **b** Case 2. **c** Case 3

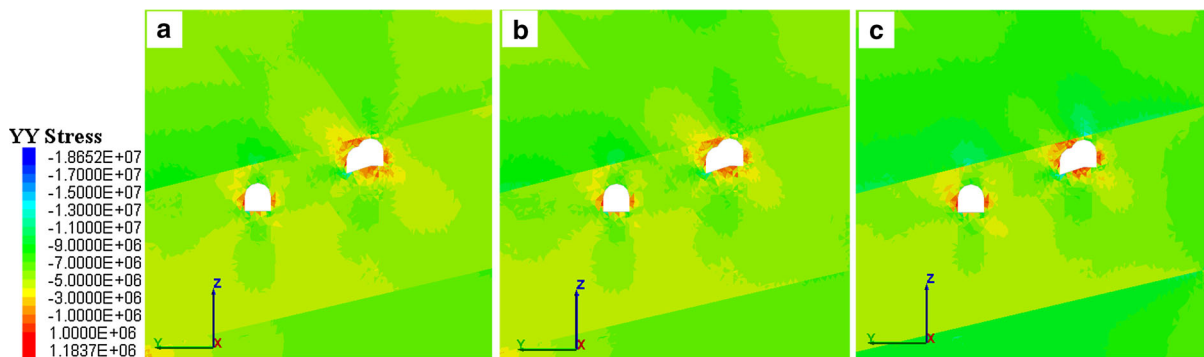


**Fig. 25** yy-stress distributions around the tunnels for different boundary conditions at the vertical cross section  $x = 0$  m (unit: Pa). **a** Case 1. **b** Case 2. **c** Case 3

no faults and no inclined layers. However, the numerical model dealt with in this paper has a fault and inclined layers with different material properties. Therefore, perfect matching for  $K_0$  cannot be expected. If matching occurs approximately, then it is a positive indicator.

Figures 26 and 27 respectively show the distributions of z-displacement and y-displacement for these cases. Z-displacements on the roof of the tunnels for case 2 are higher than those for case 1; on the other hand, z-displacements on the floor for case 2 are less than those for case 1. With respect to y-displacement, even though the results are comparable between the three cases, case 2 results seem to be closer to case 1 compared to that of case 3.

Figure 28 shows the comparisons of the failure zone around the tunnels. The results show that case 1 results are comparable to that of cases 2 and 3.

In conclusion, the numerical model reacts approximately in a similar way to case 1 and case 2 boundary

conditions. However, some minor displacement differences exist between the two cases even though the stresses at the boundaries in the two cases are almost the same. The lateral roller boundaries impose no displacement in the horizontal directions, but displacements take place at the stress boundaries. This will cause some influences on the deformation of the rock mass around the tunnels because the distance between the boundaries and tunnels is not far enough. Accordingly, the stress boundaries are more appropriate and accurate to use for the considered numerical model.

#### 4.5 Effect of Support System on the Deformation and Stability Around the Tunnels

Comparisons of the deformation and stability around the tunnels between the cases without (case 7) and with (case 9) support are covered in this part of the paper. All the plots are given with the same color legend to make accurate comparisons.

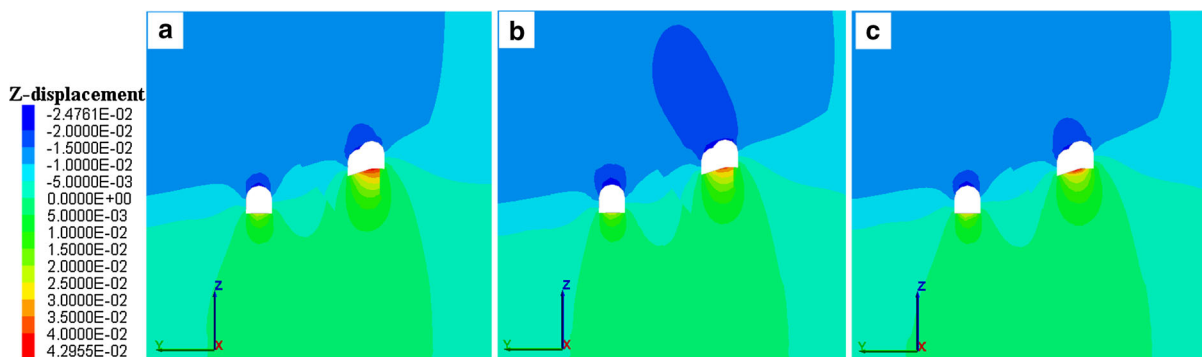


**Fig. 26** Z-displacement distributions around the tunnels for different boundary conditions at the vertical cross section  $x = 0$  m (unit: m). **a** Case 1. **b** Case 2. **c** Case 3

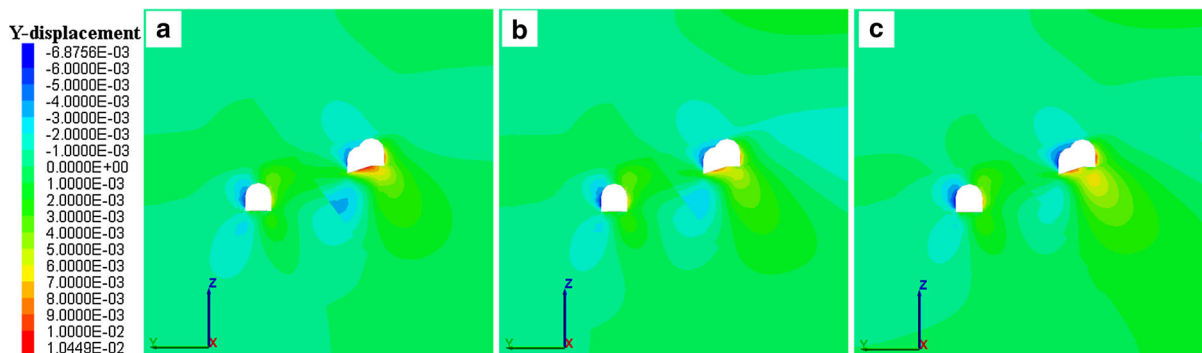


**Fig. 27** Y-displacement distributions around the tunnels for different boundary conditions at the vertical cross section  $x = 0$  m (unit: m). **a** Case 1. **b** Case 2. **c** Case 3

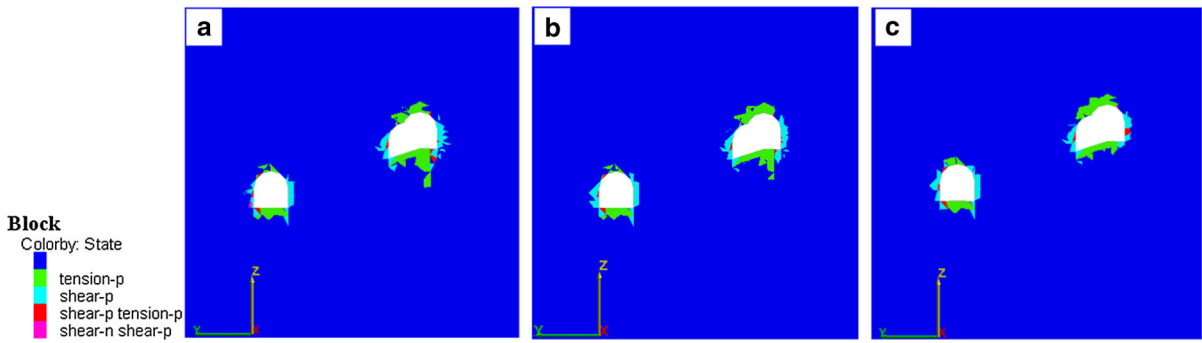


**Fig. 28** Failure zone distributions around the tunnels for different boundary conditions at the vertical cross section  $x = 0$  m. **a** Case 1. **b** Case 2. **c** Case 3

The maximum displacements obtained around the tunnels for cases 7 and 9 are given in Table 8. The maximum z-displacement on the roof decreases from 31.1 to 28.9 mm and slightly from 40.6 to 40.3 mm on the floor. This makes sense due to the fact that no support was installed on the floor. Additionally, the maximum horizontal displacement on the left wall has reduced from 33.6 to 30.5 mm; the maximum displacement on the right wall has reduced from 43.5 to 43.0 mm. The maximum distances of the failure zone

on the roof in the cases with and without support are respectively 2.31 and 2.33 m. The failed elements on the walls have also decreased after the installation of the support. The maximum distance of the failure zone on the walls decreases from 2.62 to 2.32 m. In summary, the support systems do improve the rock mass stability around the tunnels slightly.

Figure 29 provides the diagram of support axial force distribution. Majority of the bolts in the walls have reached the maximum bolt force (light blue) of

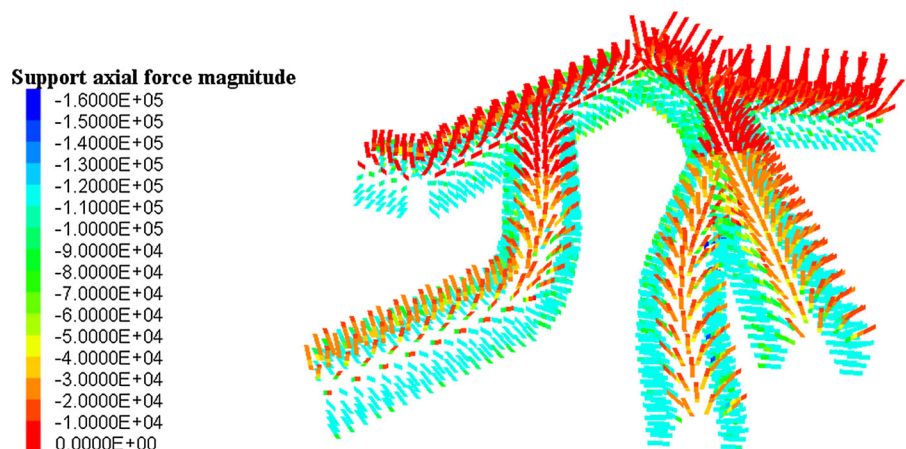
**Table 8** Effect of support system on the deformation and failure zone around tunnels

|                     | Max. z-disp. value on floor (mm) | Max. z-disp. value on roof (mm) | Max. y-disp. value on left wall (mm) | Max. y-disp. value on right wall (mm) | Max. dist. of failure zone on floor (m) | Max. dist. of failure zone on roof (m) | Max. dist. of failure zone on walls (m) |
|---------------------|----------------------------------|---------------------------------|--------------------------------------|---------------------------------------|---|--|---|
| Case 7 <sup>a</sup> | 40.6                             | 31.1                            | 33.6                                 | 43.5                                  | 1.64                                    | 2.33                                   | 2.62                                    |
| Case 9 <sup>b</sup> | 40.3                             | 28.9                            | 30.5                                 | 43.0                                  | 1.63                                    | 2.31                                   | 2.32                                    |

<sup>a</sup> Case 7 (without support)

<sup>b</sup> Case 9 (with support)

**Fig. 29** Diagram for axial force distribution of bolts and cables for case 9 (with support) (unit: Pa)



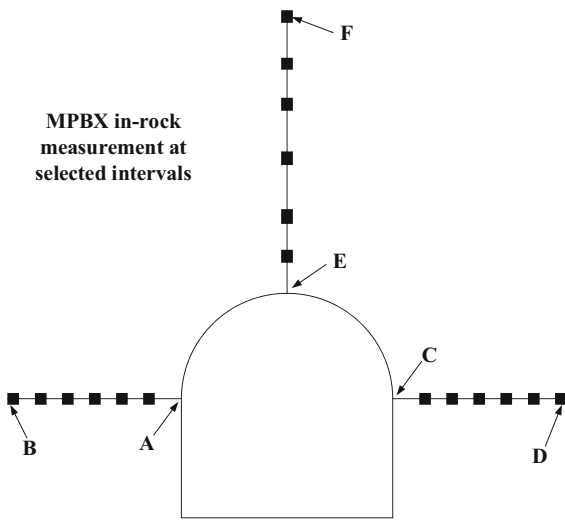


**Fig. 30** In-rock movement monitoring instruments (from the mining company)

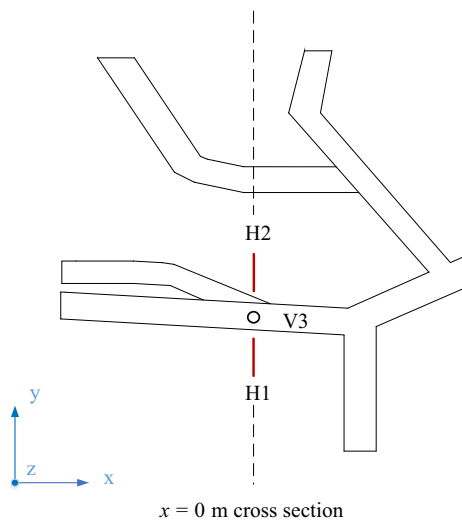


**Fig. 31** Plan view of the locations for monitoring instruments

120 KN which is the maximum tensile yield capacity of the bolts. This indicates that it is necessary to increase the bolt yield capacity or bolt density in the walls to improve the stability of the walls. Note that the length of the rock bolts in the walls is 1.83 m which is much shorter than the maximum distance of failure zone in the walls (2.32 or 2.62 m). This means that it is necessary to increase the bolt lengths to improve the stability of the walls. With respect to the bolts in the roof, the maximum tensile yield capacity of the bolts is 160 KN (dark blue). However, the number of bolts with this maximum value is small; which means that most of the roof bolts are in a safe condition. The maximum distance of the failure zone in the roof is about 2.31 m; this is less than 2.44 m, which is the length of the bolts. This length seems just sufficient.

#### 4.6 Comparison of the Results Between the Field Deformation Measurements and Numerical Predictions

Multiple point extensometers (MPBX) have been installed in this underground mine to monitor in-rock movements. Figure 30 is the cross section of the instruments. One of the instrumentation station setups has been installed inside the studied area. Each station setup consists of two horizontal extensometers (H1, H2) in the walls and one vertical extensometer (V3) in the roof of the tunnels as shown in Fig. 31.

In this study, the available maximum movements recorded by each MPBX are used, which represent the relative displacements between the head of the extensometer and the remotest anchor (e.g. A and B, C and D, E and F in Fig. 30). Table 9 shows the relative horizontal displacements (H1 + H2) and the relative roof displacement (V3) of the field

**Table 9** Comparison of displacements between field measurements and numerical simulations

| Location   | Case 3 | Case 4 | Case 5 | Case 6 | Case 7 | Case 8 | Field measurements |
|--|--------|--------|--------|--------|--------|--------|--------------------|
| Relative horizontal displacement <sup>a</sup> (mm) | 12.1   | 15.5   | 25.8   | 54.8   | 59.7   | 63.3   | 59                 |
| Relative roof displacement <sup>b</sup> (mm)       | 1.3    | 4.5    | 5.2    | 5.9    | 6.2    | 16.6   | 5.9                |

<sup>a</sup> Relative horizontal displacement = relative displacement between A and B (H1) + relative displacement between C and D (H2)

<sup>b</sup> Relative roof displacement = relative displacement between E and F (see Fig. 30 for locations of A, B, C, D, E and F)

measurements as well as the different numerical analyses results. It can be seen that the relative horizontal displacements for cases 6, 7, and 8 (strain-softening model) agree well with the field monitoring result; but the displacements of the cases using the Mohr–Coulomb model are significantly less than the field value. With respect to the relative roof movement, except for case 3 and case 8, the other cases provide more or less close values to the field displacement. Among all the comparisons, cases 6 and 7 provide the best agreement to the field values.

## 5 Conclusions

In this study, a three-dimensional numerical model was built by using available information on the stratigraphy, geological structures and mechanical properties of the rock masses and discontinuities to investigate the stability and deformation around the tunnels in an underground mine in USA. The dealt geologic system and the tunnel system were fairly complex. To thoroughly understand the geomechanical behavior of the rock mass around the tunnels, effects of several factors on stability around the tunnels were evaluated in a detailed way.

In this paper, the in situ stresses were obtained by applying proper boundary stresses to the numerical model due to the existence of inclined strata and a fault. In order to investigate the tunnel stability under different in situ stresses,  $K_0$  values of 0.5, 1.0 and 1.5 were used with the gravitational vertical stress system. Results show that the maximum vertical displacements on the roof and floor of the tunnels decrease with the increase of  $K_0$  value, while the maximum horizontal displacements on the walls increase as  $K_0$  value increases. In addition, the case with  $K_0 = 1.5$  provides the maximum failure region in the walls and roof with maximum failed distances of 1.78 and 3.23 m, making it the worst case. However, for  $K_0$  equals to 1.0, the obtained smallest range of failure zones indicates that it is the least unstable situation.

The Mohr–Coulomb and strain softening constitutive models were used to investigate the stability of the tunnels for materials with different post failure behaviors. As can be seen the degradation of strength parameters makes the model much weaker, causing larger displacements and more failed elements around the tunnels. The maximum z-displacements on the

roof, floor and the maximum y-displacement on the walls increased from 19.4, 33.7 and 19.7 to 31.1, 40.6 and 43.5 mm, respectively; the maximum distance of failure zones at these locations increased from 2.29, 1.61 and 1.52 to 2.33, 1.63 and 2.62 m, respectively. In addition, the locations with the lowest cohesion values match well with the locations which have high accumulated plastic shear strain values and they can be treated as failed elements.

Roller boundaries were compared to stress boundaries with different  $K_0$  values. Results show that the geomechanical behavior of the numerical model under the roller boundaries are closer to the stress boundaries with  $K_0$  value of 0.4, which coincides with the fact that the lateral stress ratio for roller boundary condition is for a domain without any discontinuities or inclined layers. Because the considered domain has discontinuities and inclined layers, this relation can be applied to the studied numerical model only in an approximate manner. However, because the boundaries are not sufficient far from the excavations, the roller boundaries could have influences on the deformation around the tunnels. Therefore, the stress boundaries should be applied in the considered numerical model.

The effectiveness of support system were evaluated for the case with strain-softening model and  $K_0 = 1.0$ . The maximum displacements on the roof and walls have more or less reduced when the supports were applied, but the displacements on the floor remain almost the same due to the reason that no support was installed on the floor. Under the condition without support, the maximum distances of failed region on the roof, floor and walls are respectively 2.33, 1.64 and 2.62 m. These distances decreased to 2.31, 1.63 and 2.32 m under the support system shown in Figs. 11, 12 and 13. The length of supports on the walls is less than the maximum failure distance; in addition, as shown in Fig. 29 most wall supports have reached the yield tensile capacity of supports. Therefore, it is better to add some longer cables or bolts to keep these walls safe. By contrast, roof bolts and cables seem to be adequate to keep the roof stable.

Comparisons between the field monitored movements and the numerical analyses results were made. The results show that the cases by applying the strain-softening model with  $K_0 = 0.5$  and 1.0 seem more applicable for this mine than the other cases dealt with. These findings should be useful for further numerical

analysis or research and can provide guidance for the mining company to do efficient excavations.

**Acknowledgments** The research was funded by the Centers for Disease Control and Prevention under the Contract No. 200-2011-39886. The support provided by the mining company through providing geological and geotechnical data, rock core and mine technical tours, and allowing access to the mine to perform field investigations is very much appreciated. The first author is grateful to the Chinese Scholarship Council and the University of Arizona Graduate College for providing scholarships to conduct the research described in this paper as a Visiting PhD Student (in the first year) as well as a regular Ph.D. student (in the second year) at the University of Arizona.

## References

- Aydan O, Ulusay R, Kawamoto T (1997) Assessment of rock mass strength for underground excavations. *Int J Rock Mech Min Sci* 34:18.e1–18.e17
- Barton N, Lien R, Lunde J (1974) Engineering classification of rock masses for the design of tunnel support. *Rock Mech* 6:189–236
- Chen G, Jia ZH, Ke JC (1997) Probabilistic analysis of underground excavation stability. *Int J Rock Mech Min Sci* 34:51.e1–51.e16
- Chryssanthakis P, Barton N, Lorig L, Christianson M (1997) Numerical simulation of fiber reinforced shotcrete in tunnel using the discrete element method. *Int J Rock Mech Min Sci* 34:54.e1–54.e14
- Cundall PA (1971) A computer model for simulating progressive, large-scale movements in blocky rock systems. In: *Proceedings of the international symposium rock fracture. ISRM Proceedings*, vol 2, pp 129–136
- Cundall PA (1980) UDEC-A generalized distinct element program for modelling jointed rock. Report from P. Cundall Associates to U.S. Army European Research Office, London
- Cundall PA (1988) Formulation of a three-dimensional distinct element model—part I. A scheme to detect and represent contacts in a system composed of many polyhedral blocks. *Int J Rock Mech Sci Geomech* 25:107–116
- Cundall PA, Hart RD (1992) Numerical modelling of discontinua. *Eng Comput* 9:101–113
- Fekete S, Diederichs M (2013) Integration of three-dimensional laser scanning with discontinuum modelling for stability analysis of tunnels in blocky rockmasses. *Int J Rock Mech Min Sci* 57:11–23
- Funatsu T, Hoshino T, Sawae H, Shimizu N (2008) Numerical analysis to better understand the mechanism of the effects of ground supports and reinforcements on the stability of tunnels using the distinct element method. *Tunn Undergr Space Technol* 23:561–573
- Hajiabdolmajid V, Kaiser PK, Martin CD (2002) Modelling brittle failure of rock. *Int J Rock Mech Min Sci* 39:731–741
- Hao YH, Azzam R (2005) The plastic zones and displacements around underground openings in rock masses containing a fault. *Tunn Undergr Space Technol* 20:49–61
- He ZM, Cao P (2008) Deformation and stability analysis of underground slope after excavation considering strain softening. *J Cent South Univ (Sci Technol)* 39:641–646
- Hoek E, Kaiser PK, Bawden WF (1995) Support of underground excavations in hard rock. A.A. Balkema, Rotterdam
- Itasca Consulting Group, Inc (2007) 3DEC-3 dimensional distinct element code, version 4.1
- Jiang Y, Yoneda H, Tanabashi Y (2001) Theoretical estimation of loosening pressure on tunnels in soft rocks. *Tunn Undergr Space Technol* 16:99–105
- Jiang YJ, Tanabashi Y, Li B, Xiao J (2006) Influence of geometrical distribution of rock joints on deformational behavior of underground opening. *Tunn Undergr Space Technol* 21:485–491
- Jing L (2003) A review of techniques, advances and outstanding issues in numerical modelling for rock mechanics and rock engineering. *Int J Rock Mech Min Sci* 40:283–353
- Kulatilake PHSW, Ucpirti H, Wang S, Radberg G, Stephansson O (1992) Use of the distinct element method to perform stress analysis in rock with non-persistent joints and to study the effect of joint geometry parameters on the strength and deformability of rock masses. *Rock Mech Rock Eng* 25:253–274
- Kulatilake PHSW, Wang S, Stephansson O (1993) Effect of finite size joints on the deformability of jointed rock in three dimensions. *Int J Rock Mech Sci Geomech* 30:479–501
- Kulatilake PHSW, Wu Q, Yu ZX, Jiang FX (2013) Investigation of stability of a tunnel in deep coal mine in China. *Int J Min Sci Technol* 23:579–589
- Lee YK, Pietruszczak S (2008) A new numerical procedure for elasto-plastic analysis of a circular opening excavated in a strain-softening rock mass. *Tunn Undergr Space Technol* 23:588–599
- Liu HB, Chen JT, Ming Xiao (2012) Modeling and simulation of joint zone for stability analysis of underground excavation engineering. *Procedia Eng* 37:1–6
- Nickson SD (1992) Cable support guidelines for underground hard rock mine operations. Thesis, The University of British Columbia
- Ray AK (2009) Influence of cutting sequence and time effects on cutters and roof falls in underground coal mine—numerical approach. Dissertation, West Virginia University
- Read HE, Hegemier GA (1984) Strain softening of rock, soil and concrete—a review article. *Mech Mater* 3:271–294
- Shen B, Barton N (1997) The disturbed zone around tunnels in jointed rock masses. *Int J Rock Mech Min Sci* 34:117–125
- Shreedharan S, Kulatilake PHSW (2016) Discontinuum-equivalent continuum analysis of the stability of the stability of tunnels in a deep coal mine using the distinct element method. *Rock Mech Rock Eng* 49:1903–1922
- Tan WH, Kulatilake PHSW, Sun HB (2014a) Influence of an inclined rock stratum on in situ stress state in an open-pit mine. *Geotech Geol Eng* 32:31–42
- Tan WH, Kulatilake PHSW, Sun HB (2014b) Effect of faults on in situ stress state in an open-pit mine. *Electron J Geotech Eng* 19:9597–9629
- Wang SL, Zheng H, Li CG, Ge XR (2011) A finite element implementation of strain-softening rock mass. *Int J Rock Mech Min Sci* 48:67–76

- Wang X, Kulatilake PHSW, Song WD (2012) Stability investigations around a mine tunnel through three-dimensional discontinuum and continuum stress analyses. *Tunn Undergr Space Technol* 32:98–112
- Wu Q, Kulatilake PHSW (2012a) REV and its properties on fracture system and mechanical properties, and an orthotropic constitutive model for a jointed rock mass in a dam site in China. *Int J Comput Geotech* 43:124–142
- Wu Q, Kulatilake PHSW (2012b) Application of equivalent continuum and discontinuum stress analyses in three-dimensions to investigate stability of a rock tunnel in a dam site in China. *Int J Comput Geotech* 46:48–68